

CHOIRS HI GALAXY GROUPS: THE METALLICITY OF DWARF GALAXIES

SARAH M. SWEET¹², MICHAEL J. DRINKWATER², GERHARDT MEURER³⁴, KENJI BEKKI³⁴, MICHAEL A. DOPITA⁵⁶⁷, VIRGINIA KILBORN⁸, AND DAVID C. NICHOLLS⁵

(Dated: July 2, 2014)
Draft version July 2, 2014

ABSTRACT

We present a recalibration of the luminosity-metallicity relation for gas-rich, star-forming dwarfs to magnitudes as faint as $M_R \sim -13$. We use the Dopita et al. (2013) metallicity calibrations to calibrate the relation for all of the data in this analysis. In metallicity-luminosity space we find two sub-populations within a sample of high-confidence SDSS DR8 star-forming galaxies; 52% are metal-rich giants and 48% are metal-medium galaxies. Metal-rich dwarfs classified as tidal dwarf galaxy (TDG) candidates in the literature are typically of metallicity $12 + \log(\text{O}/\text{H}) = 8.70 \pm 0.05$, while SDSS dwarfs fainter than $M_R = -16$ have a mean metallicity of $12 + \log(\text{O}/\text{H}) = 8.28 \pm 0.10$, regardless of their luminosity, indicating that there is an approximate floor to the metallicity of low luminosity galaxies. Our hydrodynamical simulations predict that TDGs should have metallicities elevated above the normal luminosity-metallicity relation. Metallicity can therefore be a useful diagnostic for identifying TDG candidate populations in the absence of tidal tails. At magnitudes brighter than $M_R \sim -16$ our sample of 53 star-forming galaxies in 9 HI gas-rich groups is consistent with the normal relation defined by the SDSS sample. At fainter magnitudes there is an increase in dispersion in metallicity of our sample, suggestive of a wide range of HI content and environment. In our sample we identify three (16% of dwarfs) strong TDG candidates ($12 + \log(\text{O}/\text{H}) > 8.6$), and four (21%) very metal poor dwarfs ($12 + \log(\text{O}/\text{H}) < 8.0$), which are likely gas-rich dwarfs with recently ignited star formation.

Subject headings: galaxies: groups – galaxies: dwarf – star formation – HI–metallicity

1. INTRODUCTION

Over the past decades, it has been shown that galaxies display an increasing metallicity with luminosity, and more fundamentally, mass (e.g. Lequeux et al. 1979; Garnett & Shields 1987; Skillman et al. 1989; Brodie & Huchra 1991; Zaritsky et al. 1994; Tremonti et al. 2004; Zahid et al. 2012). The general explanation for this relation is that two concurrent processes are at work. The first is that in the lambda cold dark matter framework, most galaxies start at the low luminosity, low metallicity end of the trendline; forming out of pristine gas clumping within dark matter (DM) haloes. Over time, DM haloes and their respective galaxies merge together to form ever-larger haloes and galaxies. The second, con-

current process is the self-enrichment of galaxies due to supernovae, with more massive galaxies retaining greater percentages of the ejecta than low-mass galaxies in the face of galactic winds (Gibson & Matteucci 1997; Kauffmann et al. 2003), and/or being more efficient at converting the enriched gas into stars (Dalcanton 2007). These two processes cause galaxies to move diagonally upwards along the trendline simultaneously towards higher mass and higher metallicity.

However, not all dwarf galaxies are formed out of metal-poor gas in their own DM halo. Tidal interactions between giant galaxies cause knots of star formation in tidal tails, which can self-gravitate without the need for a DM halo. The dwarf galaxies formed in this way are known as tidal dwarf galaxies (TDGs), and have high metallicity due to the pre-enriched matter from which they form (e.g. Mirabel et al. 1992; Duc et al. 2000; Weilbacher et al. 2003). There are a number of important implications for the study of TDGs, for example: the DM fraction within TDGs can constrain theories of gravity; the fraction of dwarf galaxies that form tidally and survive to the present day significantly affects the dwarf galaxy mass function (see e.g. Bournaud 2010).

It is not yet known what fraction of dwarf galaxies are TDGs; between ‘several’ (Bournaud 2010) and 50 per cent (Hunsberger et al. 1996) of dwarf galaxies are predicted to form in a tidal manner. This is still an open

¹ sarah@sarahsweet.com.au

² School of Mathematics and Physics, University of Queensland, Qld, 4072, Australia

³ School of Physics, University of Western Australia, 35 Stirling Highway, Crawley, WA, 6009, Australia

⁴ International Centre for Radio Astronomy Research, ICRAR M468, 35 Stirling Highway, Crawley, WA, 6009, Australia

⁵ Research School of Astronomy and Astrophysics, Australian National University, Cotter Rd., Weston ACT 2611, Australia

⁶ Astronomy Department, King Abdulaziz University, P.O. Box 80203, Jeddah, Saudi Arabia

⁷ Institute for Astronomy, University of Hawaii, 2680 Woodlawn Drive, Honolulu, HI 96822, USA

⁸ Swinburne University of Technology, Mail number H30, PO Box 218, Hawthorn, Victoria 3122, Australia

question, primarily because two TDG criteria (low DM, high metallicity) are difficult to reliably quantify. Firstly, the presence of tidal streams around currently known TDGs prevents them from reaching the virial equilibrium required for measuring total mass and confirming the presence or absence of dark matter. Secondly, the various metallicity calibrations defined in the literature yield inconsistent metallicity measurements (e.g. Kewley & Ellison 2008).

To test what fraction of dwarf galaxies form in a tidal manner, we have identified a sample of HI gas-rich groups of galaxies where there is no obvious optical interaction, but the dwarf galaxies have higher rates of star formation than expected for the group environment. This sample is ideal for locating and measuring TDGs because the past interactions in the group provide the necessary conditions for the TDGs to form, but the lack of current optical interaction means that the TDGs would be old enough for their progenitor tidal tails to have dissipated since forming them, and the TDGs would be in virial equilibrium. This allows a sound measurement of their dynamical masses and tests of theories of gravity.

Our aim is to determine the importance of tidal processes in forming dwarf galaxies in groups. In this paper we investigate the trend of metallicity with respect to luminosity of these objects in order to identify a population of candidate TDGs. Here we define ‘metallicity’ as the gas-phase oxygen abundance relative to hydrogen, $12+\log(\text{O}/\text{H})$. The following section covers the sample selection, observations and data processing. In Section 3 we present the luminosity-metallicity relation, and discuss the implications in Section 4. Our conclusions are in Section 5.

2. SAMPLE SELECTION, OBSERVATIONS, DATA PROCESSING AND MEASUREMENT

Our sample consists of galaxies in small gas-rich groups named Choir groups (Sweet et al. 2013, hereafter Paper 1). The groups were selected from the HIPASS (HI Parkes All-Sky Survey, Barnes et al. 2001), being the HI detections that were revealed by the Survey of Ionization of Neutral Gas Galaxies (SINGG, Meurer et al. 2006) to contain four or more emission line galaxies. In Paper 1, we presented a catalogue of the Choir group members and a discussion of their properties in the context of SINGG. Briefly, the Choir groups are on average more compact than groups in the Garcia (1993) catalogue, but less so than Hickson compact groups (HCGs; Hickson et al. 1989). Eight of them contain two large spirals and a number of dwarf galaxies, and as such are morphological analogues of the Local Group, albeit in a more compact state.

We observed 53 Choir member galaxies in nine groups with the integral field Wide Field Spectrograph (WiFeS, Dopita et al. 2007) on the Australian National University’s 2.3m telescope. This integral field unit has a $25'' \times 38''$ field of view with $1''$ square spaxels. The red R7000 and blue B3000 gratings (resolutions $R = 7000$ and 3000 respectively) were selected to achieve maximum velocity resolution of 45 km s^{-1} in the red arm to facilitate redshift measurements with the $\text{H}\alpha$ line, and maximum sensitivity in the blue to facilitate measure-

ment of abundance-sensitive spectral lines. The resulting wavelength ranges were 329–558 nm in the blue arm and 529–912 nm in the red. The RT560 dichroic was used to ensure that the overlapping wavelength region did not contain strong features at the expected redshifts of our sample. Table 1 lists the observing log. We found that the nod-and-shuffle observing mode provided the best sky subtraction, as it interleaves sky and object exposures to best account for time-varying sky brightness. For each run we obtained the usual set of bias frames, and for each night a set of wavelength arc, flat and ‘wire’ calibration frames. Spectrophotometric standard stars were observed nightly for each galaxy group. The data were processed using the IRAF-based pipeline described by Dopita et al. (2010).

The best-known advantage of integral field unit (IFU) spectroscopy is the acquisition of spatially-resolved spectra. However, for this study we integrate over a number of spaxels (spatial pixels) per galaxy, so instead the advantages are increased signal to noise and an improved sampling over the entire galaxy. We are conducting a full spatially-resolved kinematic and metallicity analysis of these targets and will present the results in a future paper (Sweet et al., in prep).

For the dwarf galaxies, which fit within one pointing of the $25'' \times 38''$ field of view, we integrated over a grid of spaxels containing those with $\gtrsim 3\sigma$ signal in $\text{H}\alpha$. This corresponds to 25–30 spaxels for a typical dwarf (in angular size) in our sample. For the giant galaxies, which do not fit within a single pointing, we integrated over the bright HII region nearest the centre of the galaxy. We tested the effect of different aperture sizes on measured metallicity and found that expanding the aperture to include diffuse regions of the galaxies gave consistent metallicity results with those measured only for the bright central HII region. This corresponds well with previous findings that gas-rich, star-forming dwarfs are well-mixed (Kobulnicky & Skillman 1997; Lee & Skillman 2004). We measured redshifts for each integrated spectrum and confirmed that these are not background galaxies.

We measured emission line fluxes using UHSPECFIT (Rich et al. 2010). This IDL-based program fits a Bruzual & Charlot (2003) stellar population to account for absorption, before fitting Gaussian components for each emission line. For most of the galaxies the integrated emission lines are narrow enough that a single-component Gaussian provides a good fit (see Figure 1); any residuals between the Gaussian fit and the observed spectrum are within the noise of the spectrum. For the giant galaxies that have broad components we have fit multiple Gaussian components, and again the residuals are within the spectrum noise. Reddening corrections were calculated based on the $\text{H}\alpha/\text{H}\beta$ ratio, assuming that the wavelength-dependent attenuation is due to an isothermal screen of dust, following Vogt et al. (2013, see their Appendix). Errors in flux measurements were estimated with a Monte Carlo simulation: simulated Gaussian distributions were added to random locations in the observed continuum, and the standard deviation of the measured fluxes was calculated.

Example spectra are shown in Figure 1. We present mea-

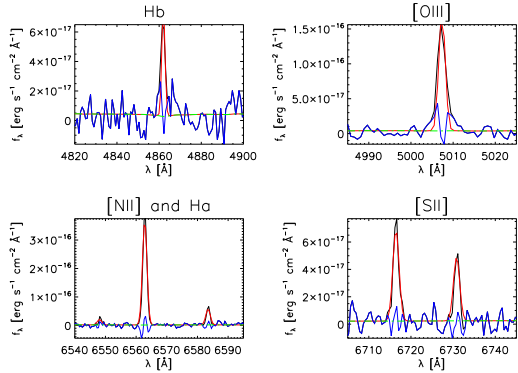


FIG. 1.— Example of emission line fitting process. We show cutouts of one WiFeS spectrum (black) in the regions of interest, with best fit from UHSPECFIT (red), fitted continuum (green dashed), and residuals (blue). This spectrum is from HIPASS J1408-21:55, the faintest dwarf in our sample.

sured fluxes in Table 2.

3. RESULTS

We constructed the luminosity-metallicity relation for our Choir member galaxies and comparison samples, using the same metallicity calibration (and where possible, reddening correction) for all of the measurements. Although the metallicity is more fundamentally related to stellar mass than to luminosity (e.g. Tremonti et al. 2004), we restricted this analysis to luminosity because of the expected large scatter in the (unknown) mass-to-light ratios of our objects, which renders it difficult to make sensible, consistent mass estimates for these galaxies. In this section, we discuss our adopted metallicity calibration and discuss our comparison samples.

3.1. Metallicity calibration

Calibrations of gas-phase metallicity typically fall into three main categories:

1. classical electron temperature and ionization correction factor technique (e.g. Peimbert & Costero 1969; Stasińska 1978, 2005),
2. recombination line method (e.g. Esteban et al. 1998; López-Sánchez et al. 2007), and
3. strong emission line (SEL) method (e.g. Pagel et al. 1979; McGaugh 1991; Kewley & Dopita 2002; Dopita et al. 2013).

Measuring electron temperature allows a ‘direct’ measurement of metallicity from strongly temperature-dependent emission lines. As such it is seen as the gold standard, but is difficult in practice because the required auroral lines (e.g. [OIII] λ 4363 Å) are weak. Further, the auroral line strengths are anticorrelated to metallicity, so are only measurable for low-metallicity galaxies. The recombination line method is also difficult, because the recombination lines are intrinsically weak. These methods are therefore reserved for bright and/or nearby galaxies. The galaxies in our sample are mostly high-metallicity, faint and not very nearby, so most do not display the

required lines for either the electron temperature or recombination line methods. Although the SEL method has limitations, which are discussed in the following paragraph, it is better suited to our sample than the other two methods. We therefore adopt the SEL method for this work.

Unfortunately, the three categories of methods give different results, so it is difficult to compare metallicities that have been calibrated with different methods. There is even wide variation within the various SEL methods, as seen in Figure 4 of Kewley & Ellison (2008). In part this is because the models are often degenerate: many, such as the oft-used R_{23} calibration (Pagel et al. 1979) have high- and low-abundance branches, determined by differences in ionization parameter q . This leads to an undefined region below the degeneracy in metallicity (López-Sánchez et al. 2012). The other major cause of discrepancy between the models is their failure to account for known physics. For instance, the models assume a Maxwellian photon energy distribution. Nicholls et al. (2012, 2013) suggested that a high-energy excess of ionizing photons could be characterised as a ‘ κ -distribution’ (generalized Lorentzian distribution). Dopita et al. (2013) have since developed a SEL model which accounts for this distribution, and encouragingly gives much more consistent results with recombination line and electron temperature methods.

Furthermore, when analysing metallicities by the SEL method, it is important to choose (i) a single metallicity calibration (so that the sample is self-consistent), that (ii) is as free of degeneracy as possible. For these reasons, we adopt the $\log [\text{OIII}]/[\text{SII}]$ vs. $\log [\text{NII}]/[\text{SII}]$ diagnostic given in Dopita et al. (2013, their Fig. 21 and our Figures 2 and 3). The diagnostic is useful because it provides a clear separation of the ionization parameter q and metallicity $12 + \log(\text{O}/\text{H})$, and is not highly dependent on the value of κ . Following Dopita et al. (2013) we adopt $\kappa = 20$. We use a bivariate polynomial interpolation to convert the diagnostic grid from line ratio to ionization parameter - metallicity space, using RMODEL (Cardiel et al. 2003)⁹. Errors in metallicity for the Choir member galaxies are estimated by RMODEL with a Monte Carlo simulation based on errors in the emission line ratios. The non-regular shape of the calibration model means that the errors are asymmetric. As expected, the errors are generally larger for fainter galaxies, and where the metallicity is low (because the low-metallicity region of the grid is the most sensitive to [NII]/[SII]).

Figure 2 illustrates our non-degenerate metallicity diagnostic with our SDSS control sample, which is presented in the following section. On that control sample, the Dopita et al. (2013) calibration is higher than the hybrid calibration method used in Tremonti et al. (2004) by 0.1-0.2 dex over the relevant magnitude range (see Fig 4). This difference was previously noted in López-Sánchez et al. (2012). Figure 3 also illustrates our metallicity diagnostic, but for our sample of galaxies.

3.2. Control samples

⁹ <http://www.ucm.es/info/Astrof/software/rmodel/rmodel.html>

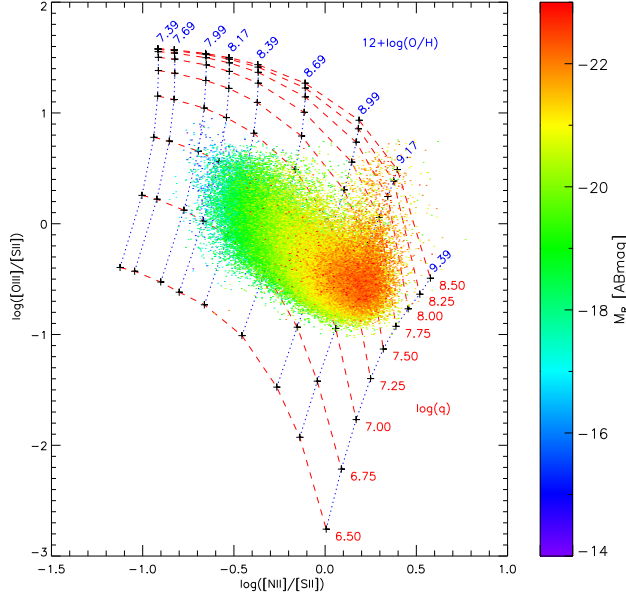


FIG. 2.— The Dopita et al. (2013) metallicity calibration grid for $[\text{OIII}]/[\text{SII}]$ vs. $[\text{NII}]/[\text{SII}]$, which illustrates the metallicity calibration for our sample. The red, dashed model curve labels depict $\log(\text{ionization parameter})$, while the blue, dotted model curve labels denote the metallicity. Here we show the galaxies in our SDSS (Aihara et al. 2011) sample, colour-coded by magnitude.

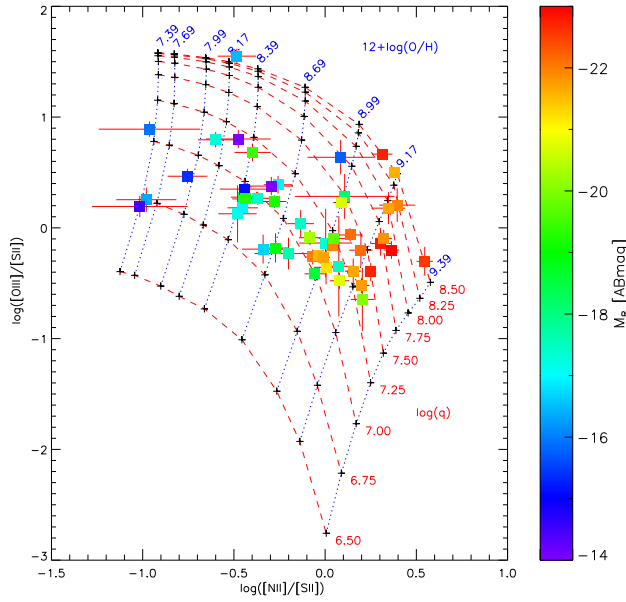


FIG. 3.— As above, for our sample of galaxies in gas-rich Choir groups.

3.2.1. SDSS

Due to availability of quality photometry and spectroscopy for 860,000 galaxies, the Sloan Digital Sky Survey Eighth Data Release (SDSS DR8, Aihara et al. 2011) is an ideal catalogue from which to draw our bright galaxy comparison sample. Following Tremonti et al. (2004), we restrict our SDSS sample to a selec-

tion of high-confidence detections. The selection limits are as follows: $0.005 < z < 0.25$; $> 5\sigma$ detection in each of $\text{H}\beta$, $[\text{OIII}]$, $\text{H}\alpha$, $[\text{NII}]$, and $[\text{SII}]$; $\log([\text{OIII}]/\text{H}\beta) < 0.61/(\log([\text{NII}]/\text{H}\alpha)-0.05)+1.3$ (to exclude AGN, following Kauffmann et al. 2003); classified as galaxy; $\sigma_z < 0.15$; $\sigma_{\text{H}\delta} < 2.5$; $\sigma_{Dn(4000)} < 0.1$. These parameters ensure that our SDSS sample is consistent with the Tremonti sample, and clean of most spurious detections. Further, we visually inspected the 300 faintest ($M_R > -16$ magnitude) galaxies and excluded 30 HII regions which were incorrectly classified as galaxies. Most of these have high metallicity ($\sim 8.6 - 9.0$) corresponding to the parent galaxy, but all of them have faint magnitudes corresponding to the local HII region, so cannot be included in the luminosity-metallicity relation. Our resulting SDSS sample contains 94,863 sources.

We then converted SDSS r -band absolute magnitude to SINGG R -band AB absolute magnitude using the r_{SDSS} to R_{Vega} transformation by Robert Lupton¹⁰ and the R_{Vega} to R_{AB} Deep Lens Survey transformation¹¹. We consider that the r -band SDSS to AB magnitude correction is small compared with the scatter in the r_{SDSS} to R_{Vega} conversion¹², so adopt the final conversion $M_{R(\text{AB})} = M_{r(\text{SDSS})} - 0.1837(g_{\text{SDSS}} - r_{\text{SDSS}}) + 0.0829$.

Using the methods described above, we performed reddening corrections and metallicity calibrations for this sample.

We plot the luminosity-metallicity relation for our SDSS sample in Figure 4. We attempt to model the luminosity-metallicity relation for SDSS using some common approaches in the literature: linear, piece-wise linear, polynomial, asymptotic fits (Tremonti et al. 2004; Kewley & Ellison 2008; Mannucci et al. 2010; Sanchez et al. 2013). It is qualitatively evident that none of these models fit the data very well, particularly at faint and/or very bright magnitudes.

Moreover, a clear turnover, or knee, can be seen in the luminosity-metallicity relation. The poor fit of the traditional fits together with the hint of multiple populations motivate us to perform Gaussian mixture modelling, which identifies sub-populations (‘clusters’) in multi-dimensional data with a maximum likelihood approach. In particular we use the unsupervised optimal fuzzy clustering algorithm described by Gath & Geva (1989), varying the number of clusters, k . It is common to measure the goodness of fit by the density of each cluster (number of members near the centre of a cluster, divided by its total number of members), but as k increases towards the sample size, the density of each cluster increases, so the fit becomes increasingly good. Instead, to avoid over-fitting, we calculate the ‘average partition density’ as defined by Gath & Geva (1989), where cluster density is normalised to the number of clusters k . We plot this as our figure of merit in Fig. 5; a larger average partition density represents a better fit. Clearly, the optimum number of clusters is $k=2$. We plot the 1-, 2- and 3- σ ellipses for these two sub-populations in Fig 6. There

¹⁰ <http://www.sdss.org/dr5/algorithms/sdssUBVRITransform.html>

¹¹ <http://dls.physics.ucdavis.edu/calib/vegaab.html>

¹² <http://www.sdss.org/dr5/algorithms/fluxcal.html#sdss2ab>

is a metal-rich ($12 + \log(\text{O}/\text{H}) = 9.1$), ‘giant’ ($M_R = -20.7$) sub-population, containing 52% of the sample, and a metal-medium ($12 + \log(\text{O}/\text{H}) = 8.5$), ‘medium+dwarf’ ($M_R = -19.5$) sub-population, with the remaining 48%. The overlap in luminosity-metallicity space suggests that there are other dimensions that may distinguish between the sub-populations, such as ionization parameter q . The fact that the knee is also seen in the calibration grid in Fig. 2 lends support to this idea. Here, low luminosity galaxies (blue-green; $M_R \lesssim -21$) have increasing metallicity but fairly constant ionization parameter ($\log q \sim 6.7-7$), then brighter galaxies (yellow-red; $M_R \gtrsim -21$) have increasing metallicity and increasing ionization parameter (up to $\log q = 8$). This combination of increasing metallicity and ionization parameter was also found in a spaxel analysis of a sample of luminous infrared galaxies by Dopita et al. (in press).

At magnitudes brighter than $M_R \sim -16$, SDSS is an ideal control sample due to the volume and quality of data (see Fig. 6). At magnitudes fainter than $M_R \sim -16$, there are two possible concerns with the SDSS control sample, which we address here. (i) There is an apparent metallicity floor to the SDSS population, with no metallicities lower than approximately $12 + \log(\text{O}/\text{H}) = 7.9$. For SDSS dwarfs fainter than $M_R \sim -16$, metallicity is constant with luminosity, with a mean of $12 + \log(\text{O}/\text{H}) = 8.28 \pm 0.10$. We note that this floor is also seen (albeit less obviously, due to different figure scale and limits) in Tremonti et al. (2004) and Fig. 21 of Dopita et al. (2013). This floor is not an artifact of the metallicity calibration, because the calibration is well-defined down to $12 + \log(\text{O}/\text{H}) = 7.39$ and is not degenerate. Moreover, the floor is not absolute since we observe Choir (and other) galaxies below this metallicity, and these are calibrated using the same method. Finally, the metallicity floor cannot be explained by selection effects. Although one may consider low surface brightness dwarfs, with few HII regions and low metallicity, to be selected against in our sample due to low signal-to-noise ratio, we see the same floor even without signal-to-noise cuts. We point out that the floor could be an artefact the aperture effect in SDSS whereby faint, nearby objects are large in angular size compared with the fibres. The SDSS measurements are consequently of nuclear spectra for these galaxies, which are higher than the mean galaxy abundance due to galactic abundance gradients. We therefore consider for this analysis that it is probably a true lower limit for the nuclei of typical galaxies, and will investigate the floor further in a future work. The exceptions to this limit are discussed in Section ??.

(ii) There is an increased dispersion in metallicity at magnitudes fainter than $M_R \sim -16$. The SDSS sample is selected to only contain high-confidence detections, so the dispersion is a physical dispersion in the galaxies, rather than caused by measurement error. We conclude that the SDSS sample is therefore of sufficient quality to act as a control sample for our population of dwarfs fainter than $M_R \sim -16$.

3.2.2. Additional dwarf galaxy control samples

We now turn to a number of other samples for which [OIII], [NII] and [SII] data are available. Where H α

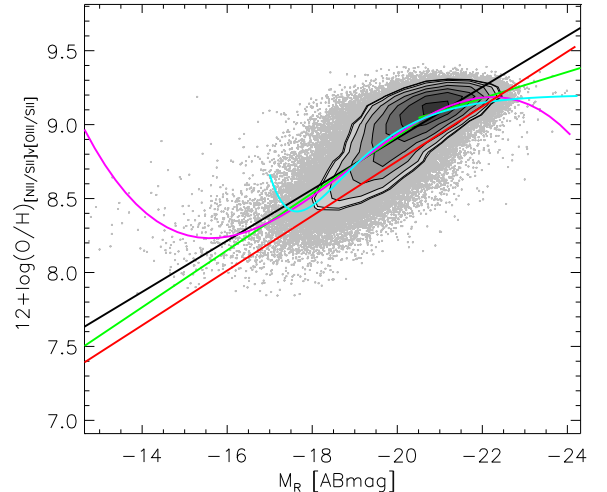


FIG. 4.— Luminosity-metallicity relation for our SDSS control sample - grey points and grey-scale contours. We overlay various fits: linear=black, piecewise linear=green, cubic=magenta, asymptotic=cyan, Tremonti linear=red. The linear fit using the Dopita et al. (2013) calibration is 0.1-0.2 dex above the Tremonti et al. (2004) fit.

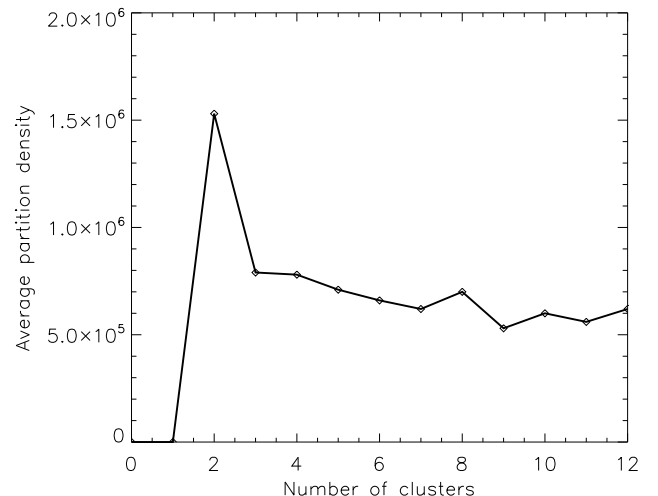


FIG. 5.— Figure of merit showing goodness of fit as a function of number of sub-populations (‘clusters’) fitted for in our SDSS control sample. The goodness of fit is measured by average partition density, which is defined as the sum of memberships near centres divided by the volume of clusters, normalised to the number of clusters. The optimum number of clusters is clearly two.

and H β are also available and the observed fluxes are given we apply the same reddening correction as for the Choirs and SDSS samples. Where these are unavailable we adopt the dereddened fluxes given by the authors. Where necessary, we convert from B - or K -band magnitudes assuming typical colours $B - R \approx 1$ and $R - K \approx 2$ (Binney & Merrifield 1998).

We include two dwarfs from the small, isolated, gas-rich, irregular dwarf galaxy sample (SIGRID, Nicholls et al. 2011), that have also been measured with the WiFeS integral field spectrograph. Full details are presented in Nicholls et al. (2014). We include additional HII regions

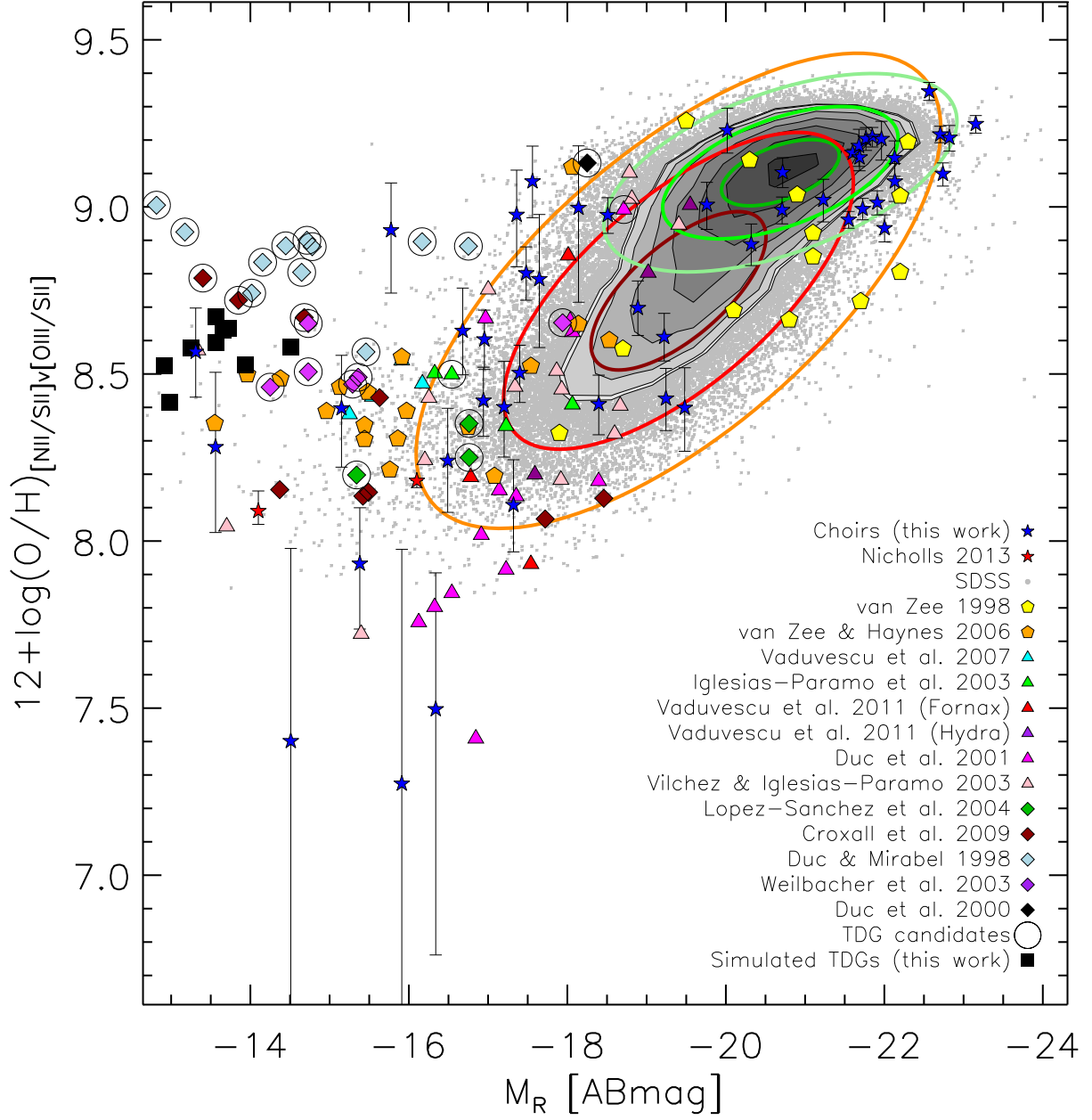


FIG. 6.— Luminosity-metallicity relation for our SDSS control sample, with Gaussian mixture modelling overlaid; the two sub-populations are shown in red and green 1-, 2-, 3- σ ellipses. Choir galaxies are shown in blue stars. Other dwarf galaxies in the literature are also shown; pentagons denote isolated galaxies, triangles denote gas-rich galaxies, and diamonds denote dwarf galaxies very near a host. Tidal dwarf galaxy candidates are circled; on average these are elevated above the normal relation defined by the SDSS sample. We also show our TDGs from our hydrodynamical simulations as black squares. Our Choir galaxies have a wide range in metallicity; three of these are significantly above the normal SDSS relation and are therefore strong TDG candidates.

and isolated dwarfs from van Zee et al. (1998) and van Zee & Haynes (2006). For each galaxy in these three samples we sum over the emission line fluxes measured in all of the HII regions within that galaxy, before calculating line ratios and interpolating to metallicity as before. Our tests show that this gives the same result as averaging the metallicities for each HII region, consistent to within ± 0.05 dex. The integrated metallicities are then plotted against total galaxy luminosities.

The SIGRID dwarfs are plotted as red stars in Fig. 6. Both of these (KK[98] 246 and HIPASS J1609-04) are consistent with the SDSS sample.

The van Zee et al. (1998) and van Zee & Haynes (2006) galaxies are shown as pentagons in Fig. 6. The bright galaxies are consistent with the SDSS sample, but the faint end is elevated in metallicity above SDSS, at a constant metallicity with luminosity ($12 + \log(\text{O}/\text{H}) = 8.46 \pm 0.04$). We note that Fig. 21 of Dopita et al. (2013) also indicates a similar discrepancy between SDSS and the van Zee & Haynes (2006) sample. At the low-metallicity end of the diagnostic, the metallicity is almost entirely determined by the $[\text{NII}]/[\text{SII}]$ ratio. This means that metallicities are dependent on the assumed relationship between N/O and $12 + \log(\text{O}/\text{H})$. The N/O relationship has been recalibrated for the Dopita et al. (2013) model grids, so metallicities measured with these models will be offset from metallicities measured with earlier models. However, we have used the recalibrated model for all of the samples in this analysis, so this recalibration of N/O does not cause the elevation of the van Zee et al. (1998) and van Zee & Haynes (2006) samples over SDSS.

We plot dwarf galaxies belonging to various local clusters as triangles in Fig. 6: Virgo (Vaduvescu et al. 2007; Vilchez & Iglesias-Páramo 2003), Hercules (Iglesias-Páramo et al. 2003), Fornax (Vaduvescu et al. 2011), and Hydra (Vaduvescu et al. 2011; Duc et al. 2001). In general, these objects tend towards lower metallicity with faint luminosity. Vaduvescu et al. (2007) found that the HI gas-richness of dwarfs has an effect on their metallicity. This is borne out by the general trend of these gas-rich cluster dwarfs (particularly the Hydra dwarfs in Duc et al. (2001)) towards very low metallicities, compared with the isolated samples, which are not gas-rich.

Finally, we also include a selection of dwarfs in groups, plotted as diamonds: NGC5291 (Duc & Mirabel 1998) and Arp245N (Duc et al. 2000) (both in pairs), the compact group HCG31 (López-Sánchez et al. 2004), the larger ~ 30 -member group M81 (Croxall et al. 2009), and various other interacting systems (Weilbacher et al. 2003).

4. DISCUSSION

4.1. Tidal dwarf galaxies

Tidal dwarf galaxies are expected to have high metallicity corresponding to the pre-enriched material from which they form. They should also be formed within a tidal tail (which may or may not be sufficiently bright to observe), without a DM halo, and may be located near their parent giant galaxy (depending on the time since formation), (e.g. Duc et al. 2000; Weilbacher et al. 2003).

Here, we use the luminosity-metallicity relation to identify candidate TDG galaxies for later follow-up.

A number of the galaxies from the existing literature shown in Fig. 6 are claimed by their authors to be TDG candidates (circled points). As for the isolated dwarf sample, these TDG candidates do not display an increasing metallicity with luminosity, but they differ from the isolated dwarf sample by showing an enhanced average metallicity ($12 + \log(\text{O}/\text{H}) = 8.70 \pm 0.05$). While some of them are clearly elevated above the luminosity-metallicity relation of SDSS bright galaxies and van Zee & Haynes (2006) isolated dwarfs (e.g. Arp245N, black diamond, Duc et al. 2000), many are consistent with the SDSS control sample (e.g. HCG31 TDG candidates, dark green diamonds, López-Sánchez et al. 2004). The overlap between isolated dwarfs (non-TDGs) and previously-identified TDG candidates is partly due to the fact that some of those TDG candidates were identified because they have a higher metallicity than normal / isolated dwarfs using different metallicity calibrations. This overlap therefore simply confirms that using different methods to measure metallicity will give different results.

4.2. Simulations

We have conducted hydrodynamical simulations of TDG candidates, the full details of which will be given in Bekki et al. (in prep., 2013). Brief details follow. We model a Milky Way-type disk galaxy with a total dark halo mass of $10^{12} M_{\odot}$, a stellar mass of $6 \times 10^{10} M_{\odot}$, bulge mass of $10^{10} M_{\odot}$, and gas mass of $3 \times 10^{10} M_{\odot}$. The adopted initial (stellar and gas-phase) metallicity gradient is -0.08 dex kpc^{-1} , with nuclear stellar metallicity of $[\text{Fe}/\text{H}] = 0.34$ dex and gas-phase metallicity $12 + \log(\text{O}/\text{H}) = 9.04$. The Milky Way-type disk galaxy is assumed to interact with a companion galaxy with the same total mass represented by a point-mass particle. The orbit of the two interacting galaxies is assumed to be hyperbolic with an initial distance of 280 kpc, orbital eccentricity of 1.1 and pericenter distance of 70 kpc. We select TDG candidates from the remnants of the interacting Milky Way-type disks as follows. We identify the newly formed stars in our simulation. For each new star we determine the number of additional new stars within 1 kpc of it, N_{ns} . For a region with $N_{ns} > 100$, the total mass of the region is $M \geq 3 \times 10^7 M_{\odot}$, so the stars in that region are considered to belong to a TDG candidate. For each selected TDG candidate, the center-of-mass is estimated by using all new stars within 1 kpc of the new star. The total mass and the mean gas-phase metallicity within 1kpc from the center-of-mass are then calculated for the TDG candidate. We assumed an R -band mass to light ratio $M/L_R = 0.86$ for a stellar population of mean age 1 Gyr and solar metallicity, using the MILES code by Vazdekis et al. (2010). Our simulated data are shown in Figure 6 as black, filled squares. The mean simulated metallicity is 8.57 ± 0.03 , within 3σ of the mean observed TDG candidate metallicity of 8.70 ± 0.05 .

4.3. Choir dwarf galaxies: tidal dwarf candidates, normal dwarfs, and very metal poor dwarfs

The Choir giants ($M_R \lesssim -20$) are in reasonable agreement with the SDSS giant sub-population, having the same metallicity, though being around one magnitude more luminous. The medium-luminosity Choir dwarfs ($-16 \lesssim M_R \lesssim -20$) are also mostly consistent with the SDSS medium-dwarf sub-population. The contours provide a simple diagnostic of the significance of any outlying results. For example, we consider that the two most metal-rich dwarfs at $M_R \sim -17.5$, being more than 3σ from the mean SDSS medium-dwarf population, are bona-fide TDG candidates.

Compared with each of the additional samples of dwarfs listed above, Choir galaxies have an increased scatter at the low luminosity end, spanning the full 1.5 dex metallicity range observed for all types of dwarfs. Some groups (e.g. HIPASS J0400-52) even span this range. The size of the error bars compared with the scatter suggests that this is not a measurement error, but either due to the calibration model or a true dispersion in the population. Figure 3 of Dopita et al. (2013) illustrates with van Zee et al. (1998) HII regions an increased scatter in metallicities between $8.0 \lesssim 12 + \log(\text{O}/\text{H}) \lesssim 8.5$ measured using this model. The metallicity calibration for these galaxies depends very strongly on the calibration between $\log(\text{N}/\text{O})$ and $\log(\text{O}/\text{H})$, as demonstrated in that figure. However, the observed dispersion is much greater in the Choir sample than in the van Zee et al. (1998) and other comparison samples, so we consider that the Choir dwarf galaxy population is inherently dispersed. We expect that this is due to a wide variation in gas content and environment (distance to host) of the Choir member galaxies.

We consider that (i) the three Choir dwarfs (J0205-55:S7, J0400-52:S8, J0400-52:S9) with metallicity above $12 + \log(\text{O}/\text{H}) = 8.6$ (3σ above the SDSS dwarfs) and above the SDSS 3σ medium-dwarf ellipse are strong TDG candidates (these candidates represent 16% of the Choir dwarfs fainter than $M_R = -18$), (ii) the dwarfs between $8.0 \lesssim 12 + \log(\text{O}/\text{H}) \lesssim 8.6$ and within the SDSS 3σ dwarf ellipse are most likely normal galaxies but still are possible TDGs, and (iii) the dwarfs (J0400-52:S2, J1051-17:S4, J1403-06:S3, J1403-06:S4) with metallicity less than 8.0 are probably the most gas-rich in our sample due to their similarity (in metallicity-luminosity space) to the gas-rich Hydra dwarfs in Duc et al. (2001) and the gas-rich HIPASS J1609-04. The very metal poor sample represents 21% of the Choir dwarfs fainter than $M_R = -18$. It could be that these very metal-poor dwarfs in our sample have acquired large amounts of relatively pristine HI gas and have had star formation re-ignited, due to recent interactions with the nearby giant galaxies (e.g., Kannappan et al. 2013). We note that Skillman et al. (2013) suggest the most metal-poor dwarfs may become metal poor due to HI gas inflowing to their central star-forming regions. Our TDG candidates and metal-poor dwarfs are noted in Table 2.

We are conducting a follow-up analysis of the kinematics and masses of our TDG candidates to determine which are bona-fide TDGs, and a further analysis of the importance of environmental location and gas content (Sweet et al., in prep).

5. CONCLUSIONS AND FUTURE WORK

In this paper we have used the new Dopita et al. (2013) metallicity calibrations to calibrate the luminosity-metallicity relation for a range of galaxy types. Importantly, we used the same calibration for our population of galaxies in HI-rich groups as for our control samples.

We make the following points:

1. In metallicity-luminosity space we find two sub-populations, or clusters, within the SDSS sample. The cluster of metal-rich giants represents 52% of the sample, while the remaining 48% are metal-poor dwarfs.
2. There is an apparent floor to the metallicity of SDSS dwarfs at $12 + \log(\text{O}/\text{H}) = 7.9$; the mean metallicity for SDSS dwarfs fainter than $M_R = -16$ is $12 + \log(\text{O}/\text{H}) = 8.28 \pm 0.10$.
3. Isolated dwarf galaxies appear to have a constant metallicity with magnitude of $12 + \log(\text{O}/\text{H}) = 8.46 \pm 0.04$, similar to the SDSS dwarf sample.
4. On average, TDG candidates from the literature have a metallicity of $12 + \log(\text{O}/\text{H}) = 8.70 \pm 0.05$, significantly elevated above SDSS galaxies. Our simulated TDGs are slightly less metal-rich than TDG candidates in the literature at $12 + \log(\text{O}/\text{H}) = 8.57 \pm 0.03$, but still significantly more metal-rich than typical dwarfs.
5. Gas-rich cluster dwarfs trend towards lower metallicity than their isolated counterparts, where Hydra dwarfs from Duc et al. (2001) have the lowest metallicity of our comparison samples, suggesting that dwarf metallicity is highly dependent on group membership.
6. At medium-bright magnitudes, our sample of star-forming galaxies in groups is consistent with SDSS.
7. At faint luminosity there is an increase in dispersion in metallicity in our sample, indicating a wide range of HI content and environmental location.
8. Based on metallicity, we identify three (16% of dwarfs) strong TDG candidates ($12 + \log(\text{O}/\text{H}) > 8.6$), which have metallicities consistent with other TDG candidates in the literature and our simulations, and significantly above the SDSS control sample at $12 + \log(\text{O}/\text{H}) = 8.28 \pm 0.10$. These galaxies are J0205-55:S7, J0400-52:S8, J0400-52:S9, and are discussed very briefly in Appendix A.1.
9. We also identify four (21%) very metal-poor galaxies ($12 + \log(\text{O}/\text{H}) < 8.0$), consistent with gas-rich cluster dwarfs whose star formation has been ignited due to interactions with nearby giant galaxies. These galaxies are J0400-52:S2, J1051-17:S4, J1403-06:S3, J1403-06:S4, and are discussed very briefly in Appendix A.2.

To conclude, metallicity can be an important diagnostic for identifying preliminary populations of candidate

TDGs. Other factors such as environment, as noted by Vaduvescu et al. (2007) may also influence metallicity, so careful follow-up is required before declaring the candidates to be bona-fide TDGs.

ACKNOWLEDGEMENTS

The authors would like to thank the anonymous referee for a constructive report, which improved the clarity of this paper.

We thank David Rohde for helpful discussions about

Gaussian mixture modelling, and Jeff Rich, Mort Canty and James R A Davenport for providing IDL routines. We acknowledge funding support from the UQ-UWA Bilateral Research Collaboration Award.

This research has made use of NASA’s Astrophysics Data System.

This research has made use of the NASA/IPAC Extragalactic Database (NED) which is operated by the Jet Propulsion Laboratory, California Institute of Technology, under contract with the National Aeronautics and Space Administration.

APPENDIX

NOTES ON STRONG TDG CANDIDATES AND VERY METAL-POOR DWARFS

Strong tidal dwarf galaxy candidates

HIPASS J0205-55:S7

This dwarf is located in Choir group HIPASS J0205-55, which appears to be comprised of two merging systems (Sweet et al. 2013). The nearest bright neighbour to S7 is S2, approximately 50 kpc away in projection. S7 has the morphology of a symmetric, edge-on disk galaxy with a half-light radius of 0.85 kpc.

HIPASS J0400-52:S8 and S9

These dwarfs are very compact with half-light radii of 1.5 and 2.5 kpc respectively. They are very close companions to S4 and S6 at only 20 kpc away in projection from their respective nearest giant galaxies. This Choir group is part of Abell 3193.

Very metal-poor dwarfs

HIPASS J0400-52:S2

This dwarf, approximately 100 kpc from its nearest neighbour S1, has a half-light radius of 1.3 kpc, and is comprised of two abutting low surface brightness knots.

HIPASS J1051-17:S4

S4 is located about 100 kpc from giant galaxy S1 in the direction of the second-brightest spiral in the group, S2. It may have gained some HI gas and had star formation reignited during a recent encounter with S1 (Kilborn et al., in prep.). It consists of two faint HII regions in a low surface brightness host with a half-light radius of 1.4 kpc.

HIPASS J1403-06:S3 and S4

These two quite compact dwarfs are the two faintest members in this Choir group. Both are located about 50 kpc from the nearby giant S1, which itself is currently interacting with the other giant in the group, S2. The interacting pair S1 and S2 is known as Arp 271. The two dwarfs each consist of a single HII region in a low surface brightness host, with half-light radii of 0.7 and 1.2 kpc for S3 and S4 respectively.

REFERENCES

- Aihara, H. et al. 2011, *The Astrophysical Journal Supplement*, 193, 29
- Barnes, D. G. et al. 2001, *MNRAS*, 322, 486
- Binney, J., & Merrifield, M. 1998, *Galactic Astronomy* (Princeton University Press)
- Bournaud, F. 2010, *Advances in Astronomy*, 2010, 1
- Brodie, J. P., & Huchra, J. P. 1991, *Astrophysical Journal*, 379, 157
- Bruzual, G., & Charlot, S. 2003, *MNRAS*, 344, 1000
- Cardiel, N., Gorgas, J., Sánchez-Blázquez, P., Cenarro, A. J., Pedraz, S., Bruzual, G., & Klement, J. 2003, *Astronomy & Astrophysics*, 409, 511
- Croxall, K. V., van Zee, L., Lee, H., Skillman, E. D., Lee, J. C., Côté, S., Kennicutt, R. C., & Miller, B. W. 2009, *The Astrophysical Journal*, 705, 723
- Dalcanton, J. J. 2007, *The Astrophysical Journal*, 658, 941
- Dopita, M., Hart, J., McGregor, P., Oates, P., Bloxham, G., & Jones, D. 2007, *Astrophysics and Space Science*, 310, 255, 0705.0287
- Dopita, M. et al. 2010, *Astrophysics and Space Science*, 327, 245
- Dopita, M. A., Rich, J., Vogt, F. P. A., Kewley, L. J., Ho, I.-T., Basurah, H. M., Ali, A., & Amer, M. A. in press, *Ap&SS*
- Dopita, M. A., Sutherland, R. S., Nicholls, D. C., Kewley, L. J., & Vogt, F. P. A. 2013, *arXiv.org*, 5950, 1307.5950
- Duc, P. A., Brinks, E., Springel, V., Pichardo, B., Weilbacher, P., & Mirabel, I. F. 2000, *The Astronomical Journal*, 120, 1238
- Duc, P. A., Cayatte, V., Balkowski, C., Thuan, T. X., Papaderos, P., & van Driel, W. 2001, *Astronomy & Astrophysics*, 369, 763
- Duc, P.-A., & Mirabel, I. F. 1998, *A&A*, 333, 813
- Esteban, C., Peimbert, M., Torres-Peimbert, S., & Escalante, V. 1998, *Monthly Notices of the Royal Astronomical Society*, 295, 401
- Garcia, A. 1993, *Astronomy & Astrophysics Supplement Series*, 100, 47
- Garnett, D. R., & Shields, G. A. 1987, *Astrophysical Journal*, 317, 82
- Gath, I., & Geva, A. B. 1989, *Pattern Analysis and Machine Intelligence*, IEEE Transactions on, 11, 773
- Gibson, B. K., & Matteucci, F. 1997, *Astrophysical Journal* v.475, 475, 47
- Hickson, P., Kindl, E., & Auman, J. R. 1989, *Astrophysical Journal Supplement Series* (ISSN 0067-0049), 70, 687
- Hunsberger, S. D., Charlton, J. C., & Zaritsky, D. 1996, *Astrophysical Journal* v.462, 462, 50
- Iglesias-Páramo, J. et al. 2003, *Astronomy & Astrophysics*, 406, 453
- Kannappan, S. J. et al. 2013, *arXiv.org*, 3292, 1308.3292v1
- Kauffmann, G. et al. 2003, *MNRAS*, 346, 1055
- Kewley, L. J., & Dopita, M. A. 2002, *The Astrophysical Journal Supplement Series*, 142, 35
- Kewley, L. J., & Ellison, S. L. 2008, *The Astrophysical Journal*, 681, 1183
- Kobulnicky, H. A., & Skillman, E. D. 1997, *ApJ*, 489, 636
- Lee, H., & Skillman, E. D. 2004, *ApJ*, 614, 698
- Lequeux, J., Peimbert, M., Rayo, J. F., Serrano, A., & Torres-Peimbert, S. 1979, *Astronomy & Astrophysics*, 80, 155
- López-Sánchez, Á. R., Dopita, M. A., Kewley, L. J., Zahid, H. J., Nicholls, D. C., & Scharwachter, J. 2012, *Monthly Notices of the Royal Astronomical Society*, 426, 2630
- López-Sánchez, Á. R., Esteban, C., García-Rojas, J., Peimbert, M., & Rodríguez, M. 2007, *The Astrophysical Journal*, 656, 168
- López-Sánchez, Á. R., Esteban, C., & Rodríguez, M. 2004, *ApJS*, 153, 243, *arXiv:astro-ph/0403182*
- Mannucci, F., Cresci, G., Maiolino, R., Marconi, A., & Gnerucci, A. 2010, *Monthly Notices of the Royal Astronomical Society*, 408, 2115
- McGaugh, S. S. 1991, *Astrophysical Journal*, 380, 140
- Meurer, G. R. et al. 2006, *ApJS*, 165, 307
- Mirabel, I. F., Dottori, H., & Lutz, D. 1992, *Astronomy and Astrophysics* (ISSN 0004-6361), 256, L19
- Nicholls, D., Jerjen, H., Dopita, M., & Basurah, H. 2014, *ApJ*, *astro-ph/1311.4152*
- Nicholls, D. C., Dopita, M. A., Jerjen, H., & Meurer, G. R. 2011, *The Astronomical Journal*, 142, 83
- Nicholls, D. C., Dopita, M. A., & Sutherland, R. S. 2012, *The Astrophysical Journal*, 752, 148
- Nicholls, D. C., Dopita, M. A., Sutherland, R. S., Kewley, L. J., & Palay, E. 2013, *The Astrophysical Journal Supplement*, 207, 21
- Pagel, B. E. J., Edmunds, M. G., Blackwell, D. E., Chun, M. S., & Smith, G. 1979, *Monthly Notices of the Royal Astronomical Society*, 189, 95
- Peimbert, M., & Costero, R. 1969, *Bulletin of the American Astronomical Society*, 1, 256
- Rich, J. A., Dopita, M. A., Kewley, L. J., & Rupke, D. S. N. 2010, *The Astrophysical Journal*, 721, 505
- Sanchez, S. F. et al. 2013, *Astronomy & Astrophysics*, 554, 58
- Skillman, E. D., Kennicutt, R. C., & Hodge, P. W. 1989, *Astrophysical Journal*, 347, 875
- Skillman, E. D. et al. 2013, *The Astronomical Journal*, 146, 3
- Stasińska, G. 1978, *Astronomy and Astrophysics*, 66, 257
- . 2005, *Astronomy and Astrophysics*, 434, 507
- Sweet, S. M. et al. 2013, *Monthly Notices of the Royal Astronomical Society*, 433, 543
- Tremonti, C. A. et al. 2004, *ApJ*, 613, 898
- Vaduvescu, O., Kehrig, C., Vilchez, J. M., & Unda-Sanzana, E. 2011, *Astronomy & Astrophysics*, 533, 65
- Vaduvescu, O., McCall, M. L., & Richer, M. G. 2007, *The Astronomical Journal*, 134, 604
- van Zee, L., & Haynes, M. P. 2006, *The Astrophysical Journal*, 636, 214
- van Zee, L., Salzer, J. J., Haynes, M. P., O'Donoghue, A. A., & Balonek, T. J. 1998, *The Astronomical Journal*, 116, 2805
- Vazdekis, A., Sánchez-Blázquez, P., Falcón-Barroso, J., Cenarro, A. J., Beasley, M. A., Cardiel, N., Gorgas, J., & Peletier, R. F. 2010, *Monthly Notices of the Royal Astronomical Society*, 404, 1639
- Vílchez, J. M., & Iglesias-Páramo, J. 2003, *The Astrophysical Journal Supplement Series*, 145, 225
- Vogt, F. P. A., Dopita, M. A., & Kewley, L. J. 2013, *The Astrophysical Journal*, 768, 151
- Weilbacher, P. M., Duc, P.-A., & Fritze-v. Alvensleben, U. 2003, *A&A*, 397, 545
- Zahid, H. J., Bresolin, F., Kewley, L. J., Coil, A. L., & Davé, R. 2012, *The Astrophysical Journal*, 750, 120
- Zaritsky, D., Kennicutt, R. C. J., & Huchra, J. P. 1994, *Astrophysical Journal*, 420, 87

TABLE 1 WiFeS observations

HIPASS+	Optical ID	RA [h m s]	Dec [d m s]	Obs. date	Int. time [s]	Mode
(1)	(2)	(3)	(4)	(5)	(6)	(7)
J0205-55:S1b	ESO153-G017	02 05 05.48	-55 06 42.54	2011/09/20	3600	N
J0205-55:S2c	ESO153-IG016	02 04 50.78	-55 13 01.55	2011/09/21	5400	N
J0205-55:S2d		02 04 50.78	-55 13 01.55	2011/09/21	5400	N
J0205-55:S3a	ESO153-G015	02 04 34.92	-55 07 09.65	2012/10/06	3600	N
J0205-55:S4a	ESO153-G013	02 04 19.75	-55 13 50.44	2011/09/20	2700	N
J0205-55:S5	APMUKS	02 04 54.77	-55 08 31.99	2011/09/12	3600	S
J0205-55:S6	APMUKS	02 04 57.07	-55 13 34.10	2011/09/22	4500	S
J0205-55:S7	6dF	02 05 00.57	-55 15 19.63	2011/09/22	4500	S
J0205-55:S8	APMUKS	02 04 29.71	-55 12 56.09	2012/10/06	3600	S
J0205-55:S9	APMUKS	02 05 23.76	-55 14 14.20	2012/10/07	4800	S
J0258-74:S1b	ESO031-G005	02 58 06.48	-74 27 22.79	2012/10/08	2700	N

J0258-74:S2	MRSS	02 58 52.43	-74 25 53.25	2012/10/08	2700	N
J0258-74:S3	2MASX	02 58 42.76	-74 26 03.55	2012/10/09	3150	N
J0258-74:S4	MRSS	02 57 29.23	-74 22 34.75	2012/10/09	4500	S
J0400-52:S1	ESO156-G029	04 00 40.82	-52 44 02.71	2012/10/07	3600	N
J0400-52:S2	APMUKS	04 00 48.07	-52 41 02.81	2012/10/07	3600	S
J0400-52:S3	2MASX	04 00 06.03	-52 39 32.63	2012/10/07	2400	S
J0400-52:S4	IC2028	04 01 18.23	-52 42 27.08	2012/07/08	3150	N
J0400-52:S5	2MASX	04 00 53.00	-52 49 38.43	2012/07/08	3150	N
J0400-52:S6	IC2029	04 01 17.84	-52 48 02.81	2012/10/09	4500	N
J0400-52:S7	APMUKS	04 01 08.99	-52 49 32.78	2012/10/09	4500	S
J0400-52:S8	-	04 01 17.00	-52 42 08.50	2012/07/08	3150	N
J0400-52:S9	-	04 01 19.29	-52 47 56.10	2012/10/09	4500	N
J1051-17:S1a	2MASX	10 51 37.45	-17 07 29.23	2011/04/30	1800	C
J1051-17:S1b		10 51 37.45	-17 07 29.23	2011/04/30	2100	C
J1051-17:S1c		10 51 37.45	-17 07 29.23	2011/04/30	2700	C
J1051-17:S2a	NGC3431	10 51 15.11	-17 00 29.44	2011/05/01	1800	C
J1051-17:S2b		10 51 15.11	-17 00 29.44	2011/05/01	1800	C
J1051-17:S3	-	10 51 35.94	-16 59 16.80	2011/04/28-29	7200	N
J1051-17:S4	-	10 51 26.01	-17 05 03.61	2011/04/29	5400	S
J1051-17:S5	-	10 51 50.91	-16 58 31.64	2011/05/01	5400	S
J1051-17:S6	-	10 51 42.78	-17 06 34.59	2011/04/30	3600	C
J1051-17:S7	-	10 51 33.36	-17 08 36.63	2011/04/30	3600	C
J1051-17:S8	-	10 51 25.92	-17 08 16.44	2011/04/29	5400	S
J1051-17:S9	-	10 51 56.54	-17 05 03.50	2012/05/18	3600	N
J1403-06:S1a	NGC5426	14 03 24.88	-06 04 09.14	2012/05/21	1650	N
J1403-06:S2a	NGC5427	14 03 26.09	-06 01 51.20	2012/05/21	1800	N
J1403-06:S2b		14 03 26.09	-06 01 51.20	2012/05/21	1800	N
J1403-06:S3	APMUKS	14 03 13.48	-06 06 24.17	2012/05/21	3600	S
J1403-06:S4	APMUKS	14 03 34.62	-06 07 59.27	2012/05/21	5400	S
J1408-21:S1a	ESO578-G026	14 08 42.04	-21 35 49.82	2012/05/20	2700	N
J1408-21:S1b		14 08 42.04	-21 35 49.82	2012/05/20	5400	N
J1408-21:S1c		14 08 42.04	-21 35 49.82	2012/05/20	4500	N
J1408-21:S1d		14 08 42.04	-21 35 49.82	2012/05/20	4500	N
J1408-21:S2	2MASX	14 08 57.72	-21 38 52.47	2012/05/18	2700	N
J1408-21:S3	2MASX	14 08 41.04	-21 37 40.97	2012/05/19	3600	N
J1408-21:S4	2MASX	14 08 33.28	-21 36 07.18	2012/05/19	3600	N
J1408-21:S5	-	14 08 39.82	-21 38 14.30	2012/05/19	9000	S
J1408-21:S6	-	14 08 52.84	-21 42 07.20	2012/05/18	3000	S/N
J1956-50:S1b		19 56 45.51	-50 03 20.29	2011/09/20	3600	N
J1956-50:S1c		19 56 45.51	-50 03 20.29	2011/09/20	5400	N
J1956-50:S1d	IC4909	19 56 45.51	-50 03 20.29	2011/09/22	5400	N
J1956-50:S1e		19 56 45.51	-50 03 20.29	2011/09/22	5400	N
J1956-50:S2	2MASX	19 55 53.21	-50 02 10.82	2011/09/21	3600	N
J1956-50:S3	-	19 56 08.20	-50 02 21.56	2011/09/21	5400	S
J1956-50:S4	-	19 55 45.92	-50 06 15.50	2011/09/22	5400	S
J2027-51:S1a	ESO234-G032	20 28 06.39	-51 41 29.83	2011/04/30	3600	C
J2027-51:S1b		20 28 06.39	-51 41 29.83	2011/04/29-30	4200	C
J2027-51:S1c		20 28 06.39	-51 41 29.83	2011/04/30	3600	C
J2027-51:S2a	ESO234-G028	20 27 31.97	-51 39 20.81	2011/09/19	3600	N
J2027-51:S2c		20 27 31.97	-51 39 20.81	2011/09/19	3600	N
J2027-51:S3	MRSS	20 27 48.52	-51 44 19.35	2011/04/28	6600	N
J2027-51:S4	-	20 27 54.64	-51 38 04.52	2011/04/29	5400	S
J2318-42a:S1c	NGC7582	23 18 23.44	-42 22 11.94	2012/05/21	1350	N
J2318-42a:S1d		23 18 23.44	-42 22 11.94	2012/05/21	900	N
J2318-42a:S2a	NGC7590	23 18 54.78	-42 14 18.94	2012/05/20	1800	N
J2318-42a:S2b		23 18 54.78	-42 14 18.94	2012/05/20	1800	N
J2318-42a:S3a	NGC7599	23 19 21.14	-42 15 24.6	2012/05/21	1800	N
J2318-42a:S3b		23 19 21.14	-42 15 24.6	2012/05/21	1800	N
J2318-42a:S4	APMUKS	23 18 50.44	-42 23 50.30	2012/05/19	5400	S

Columns: (1): SINGG name with (a-e) appended for pointing where applicable; (2): name assigned to group as found in NASA/IPAC Extragalactic Database (NED; <http://ned.ipac.caltech.edu/>); (3): J2000 right ascension of brightest source in field; (4): J2000 declination of brightest source in field; (5): Date of observations; (6): Total integration time; (7): Mode of observation. N denotes nod and shuffle, S denotes sub-aperture nod and shuffle, C denotes classical observation.

TABLE 2 Measured emission line fluxes and other quantities

HIPASS+	H β	[O III]	H α	[N II]	[S II]	[S II]	12+log(O/H)	M _R	V _{hel}
(1)	4861.3	5006.9	6562.8	6583.4	6716.4	6730.8	(8)	[mag]	[km s ⁻¹]
(2)	(3)	(4)	(5)	(6)	(7)	(10)			
J0205-55:S1	1560±140	337±85	6000±378	3110±200	531±51	371±23	9.35± ^{0.03} _{0.04}	-22.57±0.22	6490
J0205-55:S2	9110±810	13500±1200	29300±3000	4590±490	5120±490	3630±340	8.61± ^{0.04} _{0.07}	-19.22±0.00	5941
J0205-55:S3	423±119	436±116	2680±340	1390±190	348±80	243±30	9.20± ^{0.05} _{0.04}	-22.00±0.09	6074
J0205-55:S4	417±64	425±53	1740±113	943±62	665±46	465±24	8.94± ^{0.04} _{0.00}	-17.32±0.18	5941
J0205-55:S5***	1100±390	873±369	1220±290	154±348	0±0	0±0	0.00± ^{0.00} _{0.00}	-18.40±0.06	6216

J0205-55:S6	629±88	1470±180	2220±240	339±42	563±55	394±35	8.41± ^{0.09} _{0.14}	-15.78±1.08	5758
J0205-55:S7*	186±139	951±170	855±141	413±108	206±87	144±16	8.93± ^{0.19} _{0.19}	-17.65±0.05	5758
J0205-55:S8	1420±190	738±190	1750±270	369±129	327±61	229±32	8.78± ^{0.19} _{0.29}	-15.37±0.12	5891
J0205-55:S9	399±28	1520±140	1330±200	93±12	167±23	117±16	8.28± ^{0.26} _{0.26}	-21.55±0.12	6120
J0258-74:S1	1290±130	789±75	5760±610	1880±220	815±84	596±56	9.08± ^{0.05} _{0.08}	-19.48±0.29	4883
J0258-74:S2	864±99	2560±290	2920±440	250±41	371±58	260±40	8.40± ^{0.13} _{0.13}	-18.51±0.56	4883
J0258-74:S3	451±45	226±24	2620±230	983±89	668±61	505±46	8.98± ^{0.05} _{0.05}	-17.32±0.85	4655
J0258-74:S4	1020±100	3700±340	3490±510	175±29	403±59	303±42	8.11± ^{0.14} _{0.14}	-21.90±0.06	4838
J0400-52:S1***	280±31	4720±520	0±0	0±0	0±0	0±0	0.00± ^{0.00} _{0.00}	-15.91±0.02	10424
J0400-52:S2**	271±31	815±85	1150±120	16±9	90±13	63±6	7.27± ^{0.00} _{0.00}	-20.02±0.01	11659
J0400-52:S3	1900±620	315±177	7570±830	3020±290	1140±150	794±59	9.23± ^{0.07} _{0.07}	-22.82±0.01	11384
J0400-52:S4	305±31	159±33	1430±94	698±53	204±28	154±7	9.21± ^{0.04} _{0.04}	-22.71±0.05	9967
J0400-52:S5	1350±120	420±68	6740±300	3100±140	905±60	904±34	9.22± ^{0.02} _{0.02}	-22.13±0.06	10790
J0400-52:S6	171±29	81±24	1240±130	476±49	189±22	132±1	9.15± ^{0.05} _{0.05}	-18.89±0.13	10287
J0400-52:S7	526±105	456±114	1740±180	423±47	463±63	337±27	9.08± ^{0.11} _{0.11}	-17.36±0.08	10607
J0400-52:S8*	51±22	52±32	252±38	119±31	72±13	51±8	8.70± ^{0.08} _{0.08}	-17.56±0.07	9921
J0400-52:S9*	89±19	53±48	728±72	365±49	193±34	135±9	8.98± ^{0.08} _{0.08}	-22.16±0.21	10287
J1051-17:S1	16±11	31±11	46±11	8±8	4±7	3±0	8.96± ^{0.16} _{0.16}	-22.16±0.21	5465
J1051-17:S2	11±2	14±2	139±11	135±10	40±3	30±2	9.21± ^{0.03} _{0.03}	-21.85±0.05	5288
J1051-17:S3	167±72	255±82	273±75	101±49	29±16	48±10	9.00± ^{0.19} _{0.19}	-16.34±0.09	5969
J1051-17:S4**	94±17	196±29	394±54	15±8	67±11	47±6	7.50± ^{0.28} _{0.28}	-17.20±0.06	5465
J1051-17:S5	35±26	60±30	1540±220	176±33	373±51	261±30	8.40± ^{0.14} _{0.14}	-16.95±0.04	5465
J1051-17:S6	30±4	55±7	121±15	17±2	19±2	13±2	8.60± ^{0.09} _{0.09}	-16.94±0.12	5648
J1051-17:S7	9±1	11±1	32±4	3±0	5±1	4±0	8.42± ^{0.10} _{0.10}	-17.48±0.04	5374
J1051-17:S8	28±9	73±17	374±44	200±24	166±20	134±15	8.80± ^{0.13} _{0.13}	-16.68±0.05	5294
J1051-17:S9	99±29	109±26	507±70	131±27	176±27	123±15	8.63± ^{0.13} _{0.13}	-23.05±0.20	5582
J1403-06:S1	1290±90	301±37	3110±210	1350±90	489±39	359±24	9.20± ^{0.03} _{0.03}	-22.74±0.09	2498
J1403-06:S2	1780±160	12900±900	4820±460	5470±500	1310±120	1340±120	9.10± ^{0.03} _{0.03}	-22.74±0.10	2727
J1403-06:S3**	600±51	1460±130	1200±170	64±12	209±31	146±21	7.93± ^{0.04} _{0.04}	-14.51±0.86	2753
J1403-06:S4**	208±28	233±27	520±86	13±7	78±21	55±9	7.40± ^{0.58} _{0.58}	-23.15±0.26	2671
J1408-21:S1	2160±290	878±130	9140±540	4600±280	1080±90	966±75	9.25± ^{0.03} _{0.03}	-23.15±0.27	8694
J1408-21:S2	661±76	212±46	2780±189	1050±70	404±37	352±19	9.15± ^{0.04} _{0.04}	-20.72±0.10	8821
J1408-21:S3	887±86	258±34	3770±310	1330±120	637±62	505±30	9.10± ^{0.04} _{0.04}	-21.23±0.08	8782
J1408-21:S4	202±25	104±31	998±104	393±41	237±27	165±14	9.02± ^{0.06} _{0.06}	-13.31±0.52	9126
J1408-21:S5	204±402	428±601	654±284	101±228	119±94	83±13	8.57± ^{0.13} _{0.13}	-17.12±0.07	8778
J1408-21:S6***	336±155	15±124	329±127	0±0	0±0	0±0	0.00± ^{0.00} _{0.00}	-22.35±0.19	8672
J1956-50:S1	262±61	218±56	1570±180	631±83	172±34	126±15	9.18± ^{0.05} _{0.05}	-22.35±0.20	7610
J1956-50:S2	2170±2300	1710±190	7670±720	2110±200	1510±150	1080±100	8.89± ^{0.06} _{0.06}	-16.65±0.22	7015
J1956-50:S3	1590±160	10700±900	5070±610	110±20	198±31	139±20	8.24± ^{0.16} _{0.16}	-15.15±0.23	6375
J1956-50:S4	242±31	413±55	610±82	59±14	94±14	70±9	8.40± ^{0.18} _{0.18}	-21.73±0.29	7472
J2027-51:S1	51±5	47±4	621±33	321±16	134±8	226±14	8.99± ^{0.03} _{0.03}	-21.73±0.30	5830
J2027-51:S2	42±3	29±2	980±64	306±20	155±10	166±11	9.01± ^{0.04} _{0.04}	-21.91±0.17	5783
J2027-51:S3	1300±140	2740±280	4240±550	623±75	997±121	708±86	8.43± ^{0.09} _{0.09}	-17.40±0.15	5830
J2027-51:S4	1740±140	3080±260	5770±660	815±99	1130±130	792±86	8.50± ^{0.10} _{0.10}	-22.25±0.26	6013
J2318-42a:S1	8610±500	25400±1000	61900±2100	45100±1400	10300±300	9670±290	9.16± ^{0.01} _{0.01}	-22.25±0.27	1461
J2318-42a:S2	583±81	2300±230	5780±480	5170±390	2450±190	2110±130	8.99± ^{0.04} _{0.04}	-21.22±0.06	1481
J2318-42a:S3	2890±220	1490±130	13700±1500	3280±430	1800±220	1270±150	9.01± ^{0.07} _{0.07}	-20.15±0.29	1777
J2318-42a:S4***	88±24	29±21	213±30	222±15	16±7	34±4	0.00± ^{0.00} _{0.00}		1685

Columns: (1): SINGG name; (2-7): observed (and extinction-corrected fluxes only in electronic version) for various emission lines, in units of 10^{-17} erg s $^{-1}$ cm $^{-2}$; (8): metallicity calibrated using Dopita et al. (2013); (9) SINGG R-band absolute magnitude; (10): WiFeS heliocentric velocity. (*): TDG candidates; (**): very metal-poor dwarfs; (***): metallicity not measurable due to poor signal in one or more lines.